Research Article | Vol. 33, No. 11 / 2 Jun 2025 / Optics Express 22104
Optics EXPRESS

Nondegenerate three-photon absorption in zinc-blende semiconductors

MATTHEW REICHERT,[1,2,5] PENG ZHAO,[1,3] DAVID J. HAGAN,[1,4,*] AND ERIC W. VAN STRYLAND[1]

[1]CREOL, College of Optics and Photonics, University of Central Florida, Orlando, Florida 32816, USA
[2]Currently with CACI International, Inc., Florham Park, New Jersey 07932, USA
[3]Currently with Meta Platform Inc., Menlo Park, California 94025, USA
[4]Department of Physics, University of Central Florida, Orlando, Florida 32816, USA
[5]matthew.c.reichert@gmail.com
[*]hagan@creol.ucf.edu

Abstract: A prescription for determining the nondegenerate three-photon absorption spectrum of zinc-blende semiconductors is presented. Theoretical calculations based on third-order perturbation theory and Kane's band structure provide the nondegenerate three-photon absorption coefficient for any combination of photon energies and polarizations. The enhancement over three orders of magnitude is predicted when using extremely nondegenerate photon energies, which is greater than that predicted with two-photon absorption. A large polarization dependence is predicted for excite-probe measurements (two photons absorbed from the excitation and one from the probe), with variation between parallel and perpendicular polarizations of up to a factor of 10 with a significant spectral dependence. Experimental measurements on zinc-blende GaAs and ZnSe show excellent agreement with the predicted spectral shape, nondegenerate enhancement, and polarization dependence. In addition, wurtzite CdS also shows a large enhancement over the degenerate case.

1. Introduction

Nonlinear absorption limits the maximum usable irradiance in photonic devices, which imposes limitations on both linear and nonlinear optical applications and can lead to damage [1]. In semiconductors, three-photon absorption (3PA) is the dominant nonlinear absorption process for photon energies between one third and half the bandgap energy, where two-photon absorption (2PA) does not occur. 3PA has been shown to be a limiting factor for many applications and devices, including all-optical switching [2–4], mid-infrared supercontinuum generation [5–7], slow-light in photonic crystal waveguides [8,9], impact on THz generation [10–12], and heralded single-photon sources [13]. Although often considered an adverse effect, 3PA has also found applications in optical limiting [14], frequency-upconversion [15], and biomedical imaging [16]. Motivated by its broad impact, there has been theoretical and experimental work characterizing 3PA in a number of materials [17–19], particularly semiconductors [20–27], yet 3PA remains much less studied than 2PA. Work reported thus far has largely considered the degenerate case, where all three absorbed photons have the same energy, and typically come from a single beam. Nondegenerate 3PA (ND-3PA), where the energies of the three absorbed photons are different, may be important in devices where multiple beams at different frequencies interact, such as Raman amplifiers [28], semiconductor based optical parametric devices [29–33], supercontinuum and frequency comb sources [5], and two-photon gain in semiconductors [34].

Nondegenerate nonlinear absorption can vary drastically from its degenerate counterpart. For example, in direct-gap semiconductors the 2PA coefficient, α_2, is enhanced by over two orders of magnitude for extremely nondegenerate photon pairs (e.g., a photon energy ratio of ~10 in a excite-probe experiment) [35–38]. Similar effects have been observed in nondegenerate nonlinear

#543020 https://doi.org/10.1364/OE.543020
Journal © 2025 Received 9 Dec 2024; revised 31 Mar 2025; accepted 13 Apr 2025; published 19 May 2025

Optics EXPRESS

refraction [39]. The enhancement has led to sensitive gated detection of mid-infrared pulses [40] and CW beams [41,42] using uncooled PIN photodiodes, 3D mid-IR imaging [43], infrared chemical imaging [44], as well as the demonstration of nondegenerate two-photon gain and the proposal for its use in two-photon semiconductor lasers [34,36,45–47]. The increase in α_2 arises from two sources: (1) intermediate state resonance enhancement (ISRE) of the small photon energy with the zero energy intraband (self) transition and the large photon energy with the interband transition, and (2) the inverse frequency dependence of the interaction Hamiltonian. This 2PA enhancement was first theoretically predicted using a simple two-parabolic-band model [35], and later [38] with the more accurate eight-band model of Kane [48], which is applicable to direct gap zinc-blende semiconductors and takes into account spin degeneracy. These calculations yielded very similar results [38]. We previously applied Kane's model to degenerate 3PA (D-3PA) [22,27,49], showing the importance of quantum interference between the many pathways in the resulting 3PA spectrum, which is not captured in two-band models [20,21]. Additionally, Kane's model provides the dependence of multiphoton absorption on the relative polarization of the interacting waves which is much more important for 3PA than for 2PA [38].

To examine ND-3PA, we extend our analysis to the nondegenerate case where one photon has a different energy than the other two in anticipation of excite-probe experiments where the excitation is much stronger than the probe. Enhancement of ND-3PA might be expected to be even greater than that of ND-2PA, since the additional photon requires an additional intermediate state that may be utilized for ISRE as well as an increase in the number of transition matrix elements. We present theoretical calculations using Kane's model and experimental excite-probe measurements of the spectra and polarization dependence of ND-3PA of two zinc-blende semiconductors, GaAs and ZnSe, and wurtzite CdS. We find significant enhancement of 3PA for extremely nondegenerate photon pairs, which can exceed that of ND-2PA by over an order of magnitude.

2. Theory

The evolution of two beams, of irradiance I_a and I_b, interacting in a material exhibiting only 3PA, i.e., no linear or two-photon absorption, (in the thin sample [50,51] and slowly-varying envelope approximations [52]) follow

$$\frac{\partial I_a}{\partial z} = -\alpha_3(\omega_a;\omega_a,\omega_a)I_a^3 - 3\alpha_3(\omega_a;\omega_b,\omega_b)I_b^2 I_a - 6\alpha_3(\omega_a;\omega_a,\omega_b)I_b I_a^2 \tag{1}$$

$$\frac{\partial I_b}{\partial z} = -\alpha_3(\omega_b;\omega_b,\omega_b)I_b^3 - 3\alpha_3(\omega_b;\omega_a,\omega_a)I_a^2 I_b - 6\alpha_3(\omega_b;\omega_b,\omega_a)I_a I_b^2 \tag{2}$$

where $\alpha_3(\omega_p;\omega_q,\omega_r)$ is the 3PA coefficient. In this notation, the frequency arguments indicate loss at irradiance at frequency ω_p due to the presence of light at frequencies ω_q and ω_r. In general, the frequencies of each of the three absorbed photons may be different, meaning $\alpha_3(\omega_p;\omega_q,\omega_r)$ has a three-dimensional spectrum. The analysis here is restricted to the case where two of the three photons are at the same frequency as is experimentally accessible by two-beam excite-probe techniques. The six terms in Eqs. (1) and (2) correspond to four different 3PA processes. The first term in each equation is self-induced 3PA, where three photons are absorbed from a single beam, which can be measured by single beam techniques such as Z-scan [22–25,49,50]. The four remaining terms describe the interaction of two beams, which may have different frequencies and polarizations, and may be measured experimentally by excite-probe techniques [53]. The second term in Eq. (1) corresponds to the absorption of one photon from a beam at ω_a, and two from beam at ω_b. This process also gives the third term in Eq. (2), which has a prefactor twice as large (6 vs. 3), since twice as many photons are lost from the beam at ω_b than at ω_a. The factors of 3 and 6 in the second and third terms, respectively, result from interference of the beams [54–56] and is required to ensure that both $\alpha_3(\omega_a;\omega_b,\omega_b)$ and $\alpha_3(\omega_a;\omega_a,\omega_b) \to \alpha_3(\omega_a;\omega_a,\omega_a)$ as $\omega_b \to \omega_a$. This means the results of single beam experiments, such as Z-scan, and two-beam

Optics EXPRESS

experiments, such as degenerate pump-probe, will agree. The terms containing $\alpha_3(\omega_a; \omega_b, \omega_b)$ and $\alpha_3(\omega_b; \omega_b, \omega_a)$ originate from the same physical process, i.e., absorption of two photons at ω_b and one at ω_a, and are related by $\alpha_3(\omega_a; \omega_b, \omega_b)/\alpha_3(\omega_b; \omega_b, \omega_a) = \omega_a/\omega_b$.

From the electronic structure of a material, the absorption coefficient can be derived via Fermi's golden rule, which may be applied to one-, two-, and three-photon absorption [22,38,57,58]. This method has previously been used to calculate the 2PA and 3PA spectra of semiconductors [20–22,27,35,38], semiconductor quantum wells [59], as well as of other materials [60,61]. Looking at the case of absorbing two photons of energy $\hbar\omega_b$ and one of energy $\hbar\omega_a$, in anticipation of excite-probe experiments, the rate (per unit volume V) R_3 of 3PA is given by

$$R_3^{abb} = \frac{2\pi}{V\hbar}\sum_{i,f}\left|\sum_{j,l}\frac{\langle\psi_f|\hat{H}_a|\psi_l\rangle\langle\psi_l|\hat{H}_b|\psi_j\rangle\langle\psi_j|\hat{H}_b|\psi_i\rangle}{(E_{li}-2\hbar\omega_b)(E_{ji}-\hbar\omega_b)} + \frac{\langle\psi_f|\hat{H}_b|\psi_l\rangle\langle\psi_l|\hat{H}_a|\psi_j\rangle\langle\psi_j|\hat{H}_b|\psi_i\rangle}{(E_{li}-\hbar\omega_a-\hbar\omega_b)(E_{ji}-\hbar\omega_b)} + \frac{\langle\psi_f|\hat{H}_b|\psi_l\rangle\langle\psi_l|\hat{H}_b|\psi_j\rangle\langle\psi_j|\hat{H}_a|\psi_i\rangle}{(E_{li}-\hbar\omega_b-\hbar\omega_a)(E_{ji}-\hbar\omega_a)}\right|^2\delta(E_{fi}-\hbar\omega_a-2\hbar\omega_b) \tag{3}$$

where the E_{nm} are the differences in energy between eigenstates $|\psi_n\rangle$ and $|\psi_m\rangle$, and the Dirac delta function δ ensures conservation of energy. The summations are carried out over all possible initial states, i, final states, f, and intermediate states, j and l. This includes the case when the intermediate states j and l are the same as either i or f, since the wave functions, in general, may have mixed parity. The intermediate states j and l affect the energy denominators. For example, when $j = l = i$, $E_{ji} = E_{li} = 0$, and as $\hbar\omega_b \to 0$ (while maintaining $E_{fi} = \hbar\omega_a + 2\hbar\omega_b$) the first two terms in the summation diverge, resulting in a large enhancement in the 3PA transition rate. This effect is ISRE, and has been extensively studied for 2PA in semiconductors [35,36,38,40], organic molecules [62–65], and other materials [66]. This transition rate corresponds to the second term in Eq. (1), from which the 3PA coefficient can be expressed as

$$\alpha_3(\omega_a; \omega_b, \omega_b) = \frac{\hbar\omega_a R_3^{abb}}{3I_b^2 I_a} \tag{4}$$

Calculation of the ND-3PA spectrum may then be performed provided knowledge of the material's eigenstates and their energies. For this purpose, we use the band structure developed by Kane [48] based on **k·p** theory including the spin-orbit interaction. The model provides the energies and wave functions for four (spin degenerate) bands, three valence bands, heavy-hole (hh), light-hole (lh), and split-off (so), and one conduction band (cb) (see Fig. 1), and allows the momentum matrix elements coupling the bands to be calculated straightforwardly [22,38,48,49]. The matrix elements are given from the optical interaction Hamiltonians by (neglecting the A^2 term where A is the vector potential, see Supplement A Eq. S.14) [57]

$$\langle\psi_l|\hat{H}_a|\psi_j\rangle = i\frac{eP}{2\hbar\omega_a}\sqrt{\frac{2I_a}{\varepsilon_0 n_a c}}M_{lj}^{(a)} \tag{5}$$

where $P = \hbar(\mathbf{E}_p/2m_0)^{1/2}$, given the Kane energy parameter $\mathbf{E}_p$, and

$$M_{lj}^{(a)} = \frac{\hbar}{m_0 P}\hat{\mathbf{a}}\cdot\langle\psi_l|\mathrm{p}|\psi_j\rangle \tag{6}$$

are scaled momentum matrix elements, where $\hat{\mathbf{a}}$ is the unit vector of the field at ω_a, and $\mathbf{p}$ is the momentum operator [38] (see Supplement A, Tables S1 and S2). While all of the bands are

Optics EXPRESS

spin degenerate, the optical coupling depends on the relative spin, which we label α and β. A summary of Kane's band structure can be found in Supplement A. For further information see [38,48,67]. This allows simplification of the summations over the states in Eq. (3) to a summation over the bands and an integral over the states within each band at resonance. Furthermore, the bands are spherically symmetric in k-space as the energies only depend on $|\mathbf{k}|$, making integration in spherical coordinates convenient. This method has certain limitations as it does not allow determination of anisotropy of 3PA which requires the inclusion of more bands. The resulting expression for the ND-3PA coefficient is Eq. (7) (see Supplement A for derivation of parameters).

$$\begin{aligned}\alpha_3(\omega_a;\omega_b,\omega_b) = {} & \frac{K_3\mathbf{E}_p^3}{n_a n_b^2 \hbar\omega_a(\hbar\omega_b)^4} \\ & \iint \sum_{i,f}\left|\sum_{j,l}\frac{M_{fl}^{(a)}M_{lj}^{(b)}M_{ij}^{(b)}}{(E_{li}-2\hbar\omega_b)(E_{ji}-\hbar\omega_b)}\right. \\ & + \frac{M_{fl}^{(b)}M_{lj}^{(a)}M_{ij}^{(b)}}{(E_{li}-\hbar\omega_a-\hbar\omega_b)(E_{ji}-\hbar\omega_b)} \\ & \left. + \frac{M_{fl}^{(b)}M_{lj}^{(b)}M_{ij}^{(a)}}{(E_{li}-\hbar\omega_b-\hbar\omega_a)(E_{ji}-\hbar\omega_a)}\right|^2 \frac{k_r}{\left|\frac{\partial E_{fi}}{\partial k}\right|_{k=k_r}}\sin(\theta)\mathrm{d}\theta\mathrm{d}\phi\end{aligned} \tag{7}$$

where n_q are the (linear) refractive indices at ω_q, k_r is the electron wave number at resonance, i.e., where $E_{fi}(k_r) = \hbar\omega_a + 2\hbar\omega_b$, and

$$K_3 = \frac{1}{3}\frac{e^6\hbar^2}{\sqrt{2}\pi^2\varepsilon_0^3 c^3 m_0^{3/2}} \approx 2.158\times10^{-132} J^{11/2}m^3/W^2 \approx 5.108\times10^{-17} eV^{11/2}cm^3/GW^2 \tag{8}$$

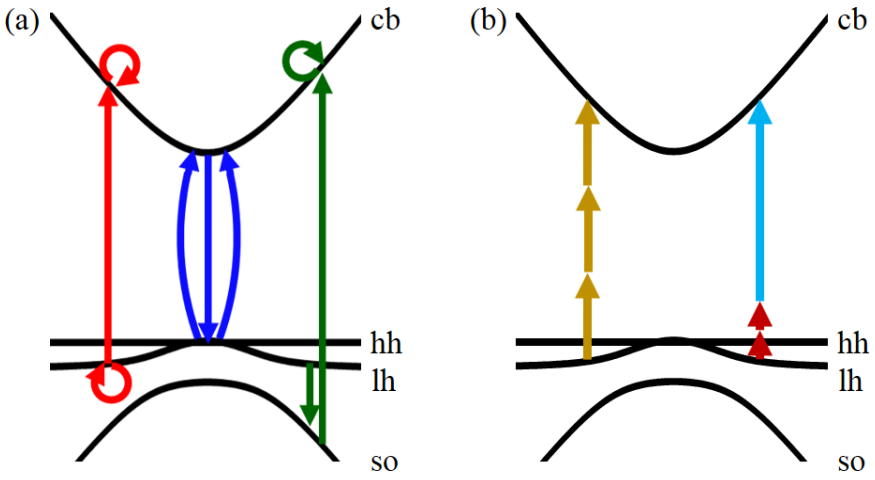

Fig. 1. Three photon absorption in zinc -blend semiconductors. Kane's band structure with one conduction band (cb), and three valence bands; heavy-hole (hh), light-hole (lh), and split-off (so) bands. (a) Colored arrows represent examples of three different quantum pathways for 3PA, from the light-hole band to conduction band (red: lh → lh → cb → cb, blue: lh → cb → lh → cb, and green: lh → so → cb → cb). (b) Comparison of photon energies (arrows) for degenerate (yellow) and extremely nondegenerate (red and blue).

Optics EXPRESS

In anticipation of excite-probe experiments where the excitation irradiance is much larger than that of the probe, and for the case of very nondegenerate frequencies so that the energy of the excitation photons is much less than the energy of the probe photons, Eq. (7), where the subscript a indicates the probe (p) and subscript b indicates the excitation (e), Eqs. (1) and 2 collapse to:

$$\frac{\partial I_p}{\partial z} = -3\alpha_3(\omega_p;\omega_e,\omega_e)I_e^2 I_p \tag{9}$$

Losses from other terms will be assumed negligible and degenerate 3PA of the excitation will not be energetically allowed.

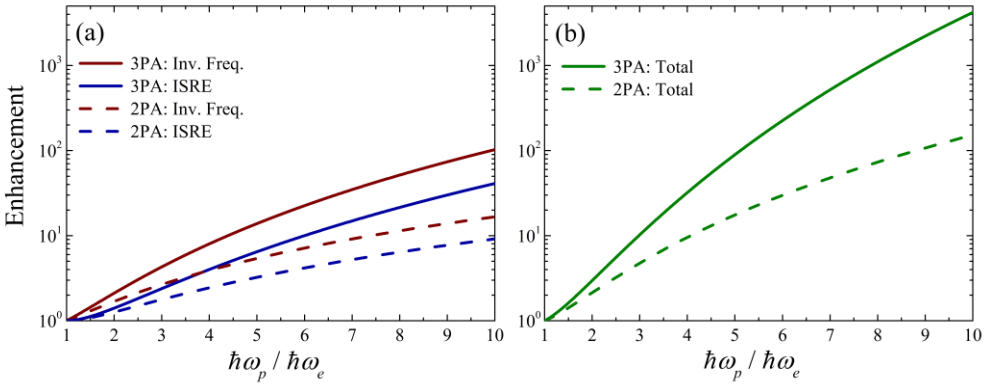

Fig. 2. Comparison of nondegenerate enhancement mechanisms for 3PA and 2PA. (a) Enhancement of (solid) 3PA and (dashed) 2PA arising from (a) (red) inverse frequency dependence of interaction Hamiltonian (Eq. (7)) and (blue) intermediate state resonance enhancement for one pathway $|l\rangle = |j\rangle = |i\rangle$ (with $E_{li} = E_{ji} = 0$). In both 2PA and 3PA, the enhancement is dominated by the frequency dependence of the interaction, contributing about twice as much as ISRE at $\hbar\omega_p/\hbar\omega_e = 10$. (b) The total enhancement is given by the product of the two mechanisms, which is well over an order of magnitude larger for 3PA (solid green) than for 2PA (dashed green) at $\hbar\omega_p/\hbar\omega_e = 10$.

It is worth examining Eq. (7) to discuss the physical origin of the enhancement when using extremely nondegenerate photon pairs. We can see two distinct effects that cause enhancement: (1) intermediate state resonance enhancement (ISRE), and (2) the inverse frequency dependence of the coupling matrix elements. Regarding effect (1); the resonance denominators within the summation over all intermediate states contribute to the enhancement when the sum of one or two photons is near the energy difference between the initial and one of the intermediate states. This effect may be thought of as follows: approaching resonance increases the time-energy uncertainty limited virtual-state lifetime allowing a longer time window for another photon to interact, thus increasing the total absorption probability. The three terms in Eq. (7), before squaring, contribute scalings of ω^{-2}, ω^{-1}, and ω^0 respectively. These terms then interfere upon squaring to give scaling from ω^{-4} to ω^0. Effect (2) is distinct, originating from the ω^{-1} dependence of the interaction Hamiltonian, and results in the $(\hbar\omega_p\hbar\omega_e{}^4)^{-1}$ factor in Eq. (7) giving an overall maximum scaling of ω^{-5} (see Eqs. (7) and SI). This effect is independent of the intermediate states used in the transition, as it depends only on the frequencies of the photons themselves. The enhancement from the interaction Hamiltonian (2) is actually greater than that of ISRE (1). The combination of these two enhancement effects yields a total scaling of α_3 of from ω^{-9} to ω^{-5}. In the nondegenerate case, we cannot take full advantage of this since we require $\omega_p + 2\omega_e \geq E_g$ so that both frequencies cannot be small. Figure 2 shows the enhancement factor from each effect for both 2PA and 3PA where we have assumed the ω^{-9} scaling dominates all other terms in Eq. (7)

Optics EXPRESS

[38], for one pathway $|l\rangle = |j\rangle = |i\rangle$ (with $E_{li} = E_{ji} = 0$). We see the greatest enhancement comes from the frequency dependence of the interaction rather than ISRE, which is true for both 3PA and 2PA. Also shown is the total enhancement, given by the product of the two contributions. At a $\hbar\omega_p/\hbar\omega_e = 10$, 2PA is enhanced by ~150×, while 3PA is enhanced by ~4200×. The actual 3PA coefficient enhancement is expected to be less than this, since it results from a weighted average over all possible pathways which interfere resulting in the overall enhancement. Regardless, the additional photon utilized in the 3PA process results in both another intermediate state, which may provide resonance enhancement, as well as an additional prefactor of $\hbar\omega_e^{-2}$, resulting in a greater enhancement of ND-3PA than of ND-2PA [36].

3. Calculation results

The ND-3PA spectrum can be calculated for any direct-gap zinc-blende semiconductor given only three energy parameters—the bandgap energy E_g, split-off energy Δ, and the Kane energy, $\mathbf{E}_\mathrm{p}$, as well as the refractive index (see Table 1). Calculations are performed in the following manner. For each transition energy E_{fi}, the corresponding value of k_r is determined from the band structure, and the coefficients of the corresponding wave functions are found (see Supplement A). The momentum matrix elements coupling each state are then calculated from [38] (see Supplement A, Tables S1 and S2), and the ND-3PA coefficient is calculated via Eq. (7).

Table 1. Semiconductor properties used for ND-3PA calculations. The full dispersion of $n(\omega)$ is used for the calculation, a numerical value listed is at $\hbar\omega = E_g/3$ is provided for reference.

Material	E_g (eV)	Δ (eV)	$\mathrm{E_p}$ (eV)	$n(\omega)$
GaAs	1.424 [68,69]	0.34 [68,69]	28.9 [70]	3.32 [71]
ZnSe	2.67 [72]	0.42 [73]	24.2 [74]	2.45 [75]
CdS	2.42 [76]	0.56 [76]	21.0 [74]	2.26 [77]

Figure 3 shows the calculated 3PA spectrum of GaAs, broken down into the contributions starting in each of the three valence bands, plotted versus the sum of the three photon's energies, $\hbar\omega_p + 2\hbar\omega_e$, and compares the degenerate and nondegenerate cases. The spectra of three dominant pathways (individual terms in Eq. (7)) from the light-hole to conduction band are shown in Fig. 3(b) and 3(d), where the blue curves correspond to: red lh → lh → cb → cb, blue lh → cb → lh → cb, and green lh → so → cb → cb, as illustrated in Fig. 1. The individual quantum pathways have different signs (i.e. relative phases) that depend on the sign of the momentum matrix elements (overlap integrals) and the sign of the energy denominator. For example, for the blue curve in Fig. 3 the matrix elements are negative (see Supplement A), but each term also has a negative denominator, since $E_{li} = E_{lh} - E_{lh} = 0$, yielding an overall positive quantity. For the green curve all the matrix elements are positive, but the energy denominators are negative since $E_{li} = E_{so} - E_{lh}$, also yielding a negative quantity. All these pathways interfere since they have the same initial and final states, resulting in the oscillatory 3PA spectrum for the light-hole band (Fig. 3(a) dotted line). The total α_3 (solid curve) is the sum of the contributions obtained starting in the light-hole (dotted), heavy-hole (dashed), and split-off band (dot-dashed).

Pathways involving three interband transitions are possible for 3PA, as indicated by the blue arrows in Fig. 1, and in fact dominate in the degenerate case near the band edge since the intraband momentum matrix elements involved in the other pathways go to zero as $k \to 0$ [20,67]. This term, the so-called allowed-allowed-allowed term, is the only one used in Wherrett's model for degenerate 3PA [20]. However, in the nondegenerate case, ISRE of intraband transitions become important and even dominant for extremely nondegenerate 3PA. In the nondegenerate case, shown in Fig. 3(c) and 3(d), $\hbar\omega_e = 0.16$ eV ($\lambda_e = 7.75$ μm), which is 11% of the bandgap energy of GaAs, and the contribution from each of the three pathways illustrated in Fig. 1 is increased

Optics EXPRESS

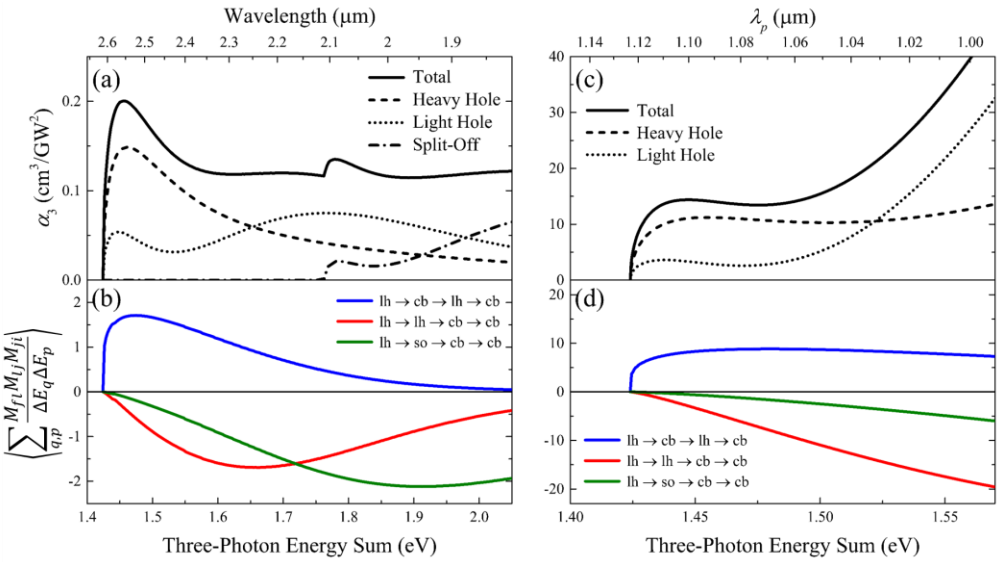

Fig. 3. Calculated 3PA spectrum of GaAs for (a) degenerate from [22,27,49] and (c) nondegenerate ($\hbar\omega_e = 0.16$ eV, $\lambda_e = 7.75$ μm) case showing contributions calculated starting in the heavy-hole (dashed), light-hole (dotted), split-off band (dot-dashed), and total (solid). Examples of contributions from individual pathways originating from the light-hole band in the (b) degenerate case from Ref. [22,27,49] and (d) nondegenerate cases. Colors in (b) and (d) correspond to pathways shown in Fig. 1. Top axis in (c) and (d) indicates the wavelength λ_p for $\lambda_e = 7.75$ μm.

from ISRE but differently in each case due to the different denominators in Eq. (7). As $\hbar\omega_p/\hbar\omega_e$ increases, while $\hbar\omega_p + 2\hbar\omega_e$ is held constant, $\hbar\omega_e$ gets closer to resonance with intraband and intervalence band transitions, and $\hbar\omega_p$ approaches resonance with interband transitions, both of which contribute to enhance 3PA. ISRE combines with the nondegenerate enhancement (photon energy prefactor in Eq. (7)), which provides an overall multiplicative enhancement factor between 240× and 360× (depending on $\hbar\omega_p$). Clearly, even larger enhancements are predicted for more nondegenerate photon energies, but eventually becomes limited by competing two-photon and linear absorption. We note that the overall enhancement is significantly reduced by the quantum interference between the various pathways.

Figure 4 shows the calculated ND-3PA spectrum of GaAs plotted versus the sum of the three photons' energies, $\hbar\omega_p + 2\hbar\omega_e$. Figure 4(a) displays the entire spectrum in a 3D color scale plot versus the nondegeneracy, i.e., the ratio of the photon energies $\hbar\omega_p/\hbar\omega_e$ (also shown in 2D color plot in Fig. 4(b)). For a fixed photon energy sum, increasing the ratio $\hbar\omega_p/\hbar\omega_e$ results in an enhancement of α_3 by over three orders of magnitude. Within the gray shaded region $\hbar\omega_p + \hbar\omega_e > E_g$, and ND-2PA dominates making ND-3PA experimentally inaccessible. Figure 4(c) shows curves of α_3 for degenerate ($\hbar\omega_p = \hbar\omega_e$) and three nondegenerate cases with fixed $\hbar\omega_e$, where α_3 is the smallest for degenerate ($\hbar\omega_p/\hbar\omega_e = 1$) and increases as the excitation photon energy decreases ($\hbar\omega_p/\hbar\omega_e$ increases). The nondegenerate enhancement for a nongedeneracy $\hbar\omega_p/\hbar\omega_e = 10$ is up to ~80× near 1.45 eV to over 400× near the 2PA edge (1.58 eV). Beyond the 2PA edge, the theory predicts extremely high ND-3PA near strong resonances due to resonance between valence bands. For example, the peak at a nondegeneracy of about 3 for three-photon energy sums greater than 1.8 eV correspond to intermediate state resonances between the split-off and heavy-hole bands. This region of the spectrum, however, is where 2PA occurs, since here $\hbar\omega_p + \hbar\omega_e > E_g$, as indicated in Fig. 4(b), which may dominate.

Optics EXPRESS

Furthermore, other fifth-order nonlinear effects are not included in the theory presented here (e.g., Stark effect, electronic Raman, etc.), which will affect any calculations of 5th-order nonlinear refraction, [78] and the band model used does not capture broadening effects which are expected to reduce the ND-3PA amplitude. Such effects will ultimately limit applicability for even greater nondegeneracies, along with single-photon absorption as one of the photon energies approaches the bandgap. Even so, this region may offer interest for further study.

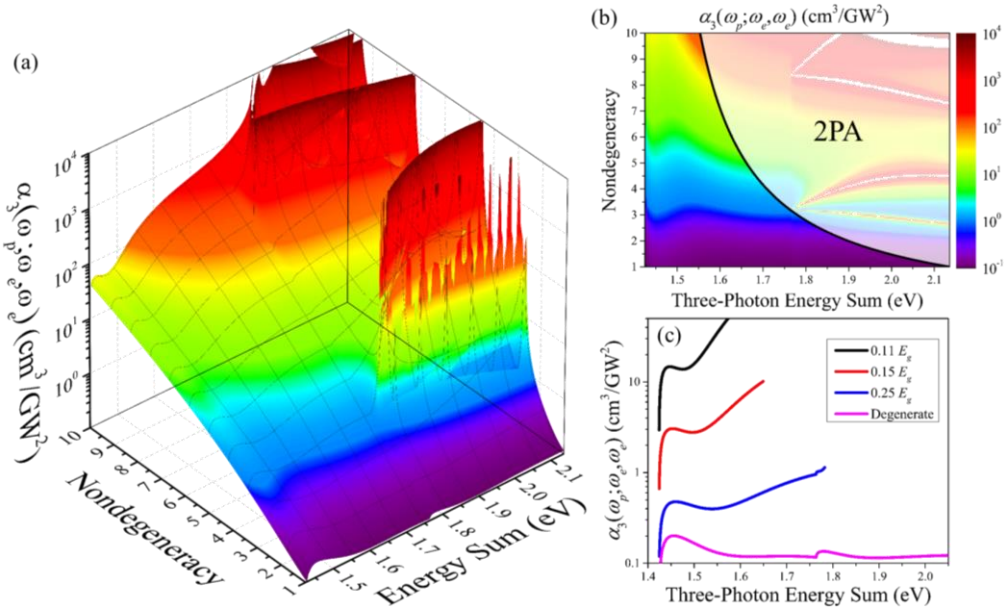

Fig. 4. Calculated ND-3PA spectrum of GaAs. (a) 3D plot of $\alpha_3(\omega_p; \omega_e, \omega_e)$ versus photon energy sum and photon energy ratio or nondegeneracy (colored vertical scale). This graph includes regions where 2PA is allowed. Note spikiness about a nondegeneracy of 3 between 1.8 and 2.15 eV is a numerical artifact due under sampling. (b) shows 2D projection with shaded region indicating where ND-2PA is allowed (upper right portion delineated by solid black line). (c) α_3 for (magenta) degenerate, and fixed $\hbar\omega_e$ of (blue) 0.36 eV, (red) 0.21 eV, and (black) 0.16 eV. Curves are truncated at the onset of ND-2PA, i.e., where $\hbar\omega_p + \hbar\omega_e = E_g$.

The dependence of α_3 on the polarization of the probe with respect to that of the excitation may be determined since the momentum matrix elements in Kane's model depend on the relative orientation of the fields [38]. Figure 5 shows the 3PA coefficients for perpendicular polarizations, where the x-component of the momentum matrix elements is used for the probe, while the z-component is used for the excitation [38] (see Supplement A). Compared to the case of parallel polarizations, $\alpha_{3,\perp}$ is significantly reduced near the band edge particularly in the degenerate case, while still retaining spectral features similar to $\alpha_{3,\parallel}$ at higher transition energies (c.f., Fig. 3). This behavior is different than for 2PA, where $\alpha_{2,\perp}$ exhibits a nearly identical spectrum to $\alpha_{2,\parallel}$, simply reduced by a factor of 2-3 [38]. The ratio $\alpha_{3,\parallel}/\alpha_{3,\perp}$ is predicted to increase near the band edge, most strikingly in the degenerate case. Both nondegenerate and ISRE mechanisms are independent of polarization, and thus we observe similar enhancement behavior for nondegenerate photons in Fig. 5(c) and 5(d).

Optics EXPRESS

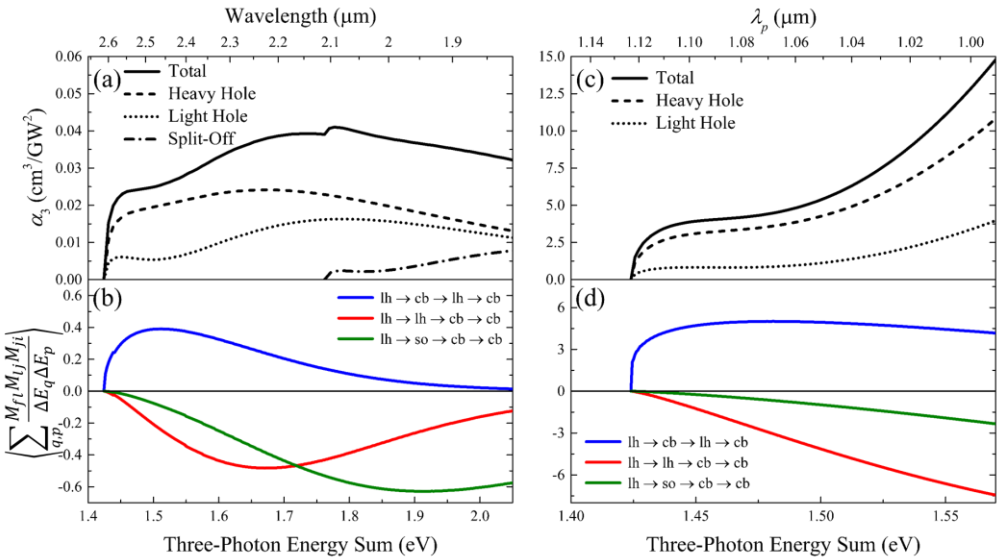

Fig. 5. Calculated 3PA spectrum of perpendicular polarizations for (a) degenerate and (c) nondegenerate ($\hbar\omega_e = 0.16$ eV, $\lambda_e = 7.75$ μm) in GaAs for (dashed) heavy-hole, (dotted) light-hole, (dot-dashed) split-off bands, and (solid) total. Examples of contributions from individual pathways originating from the light-hole band in the (b) degenerate case from [22,27,49] and (d) nondegenerate cases. Colors in (b) and (d) correspond to pathways shown in Fig. 1. Top axis in (c) and (d) indicates the wavelength λ_p for $\lambda_e = 7.75$ μm.

4. Experiment

We measure ND-3PA via excite-probe experiments (see Fig. 6) using a 1 kHz commercial Ti:sapphire chirped-pulse-amplifier laser system (Legend Elite Duo HE+, Coherent) that pumps optical parametric generators/amplifiers (TOPAS-800 and HE-TOPAS, Light Conversion). Depending on the sample, either the idler or difference frequency of the signal and idler, generated in an external $AgGaS_2$ module, is used as the excitation. A white-light continuum is created by focusing a small portion of the 800 nm laser fundamental into either a 5 mm thick sapphire plate or 10 mm cuvette filled with water, which is spectrally filtered (10 nm FWHM) for use as the probe. Variation in the probe transmission is measured synchronously at the modulation frequency of an optical chopper in the excitation beam using a lock-in amplifier (SR830, Stanford Research Systems) as the temporal delay between the pulses is varied by a delay line in the probe beam path. Linear polarizations of both beams are maintained by polarizers, and a half-wave plate is used to adjust the angle of the probe's polarization. To ensure that 3PA causes the observed transmission change, we ensure a quadratic dependence on the excitation irradiance by conducting measurements at multiple excitation energies that is changed using a half-wave plate and polarizer combination. For measurements of ZnSe and CdS, as reported in [39], the irradiance was calibrated using beam deflection measurements [39,79–81] of fused silica, which is assumed to have $n_2 = 2.5 \times 10^{-19}$ m^2/W [82].

3PA is a (nearly) instantaneous process, meaning absorption only occurs when the two pulses are temporally overlapped within the sample. For nondegenerate measurements with very different excitation and probe wavelengths, group velocity mismatch (GVM) causes significant temporal walk-off. Following Negres, *et al.* [53], we derive an analytical expression for the electric field distribution at the back surface of the sample that includes GVM effects. We are interested in the evolution of the weak probe field defined by $\boldsymbol{E}_p(\mathbf{r}, z, t) = \frac{1}{2}E_p(\mathbf{r}, z, t)\exp[i(k_p z - \omega_p t)]\hat{\mathbf{p}} + \text{c.c.}$,

Optics EXPRESS

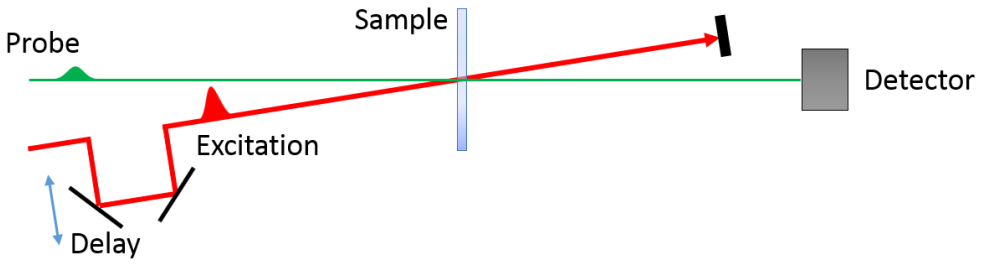

Fig. 6. Schematic of excite-probe experimental setup

where E_p is the field amplitude, $\mathbf{r}$ is the transverse radial coordinate, $k_p = n_{0,p}\omega_p/c$, and $\mathbf{p}\hat{}$ is the polarization unit vector of the probe. Within the slowly varying envelope approximation (SVEA) [52], the nonlinear wave equation governing the probe's evolution in the presence of a strong excitation with ND-3PA is (see Supplement B for derivation)

$$\frac{\partial E_p}{\partial z} + \frac{1}{v_p}\frac{\partial E_p}{\partial t} = \frac{3}{2}\alpha_3(\omega_p;\omega_e,\omega_e)I_e^2 E_p \tag{10}$$

where v_p is the probe's group velocity, I_e is the excitation irradiance, and we have assumed the sample to be thin [50] and the excitation undepleted [53]. Assuming temporally Gaussian pulses the probe field at the back surface of the sample is [39,53]

$$E_p = E_{p,0}\exp\left(-\frac{(T-T_d-\rho)^2}{2(\tau_p/\tau_e)^2} - \frac{3\sqrt{2\pi}}{8\rho}\alpha_3 L I_{e,0}^2\{erf[\sqrt{2}T] - erf[\sqrt{2}(T-\rho)]\}\right) \tag{11}$$

where $E_{p,0}$ is the input probe field distribution, $T = (t - z/v_e)/\tau_e$ is normalized time in the frame of the excitation pulse, τ_p and τ_e are the probe and excitation pulse durations (HW1/eM), T_d is the normalized delay, L is the sample thickness, and $I_{e,0}$ is the peak excitation irradiance distribution. The GVM parameter, ρ, which characterizes the temporal walk-off, is

$$\rho = \frac{L}{\tau_e}\left(\frac{1}{v_p} - \frac{1}{v_e}\right) = \frac{L}{\tau_e c}(n_{g,p} - n_{g,e}) \tag{12}$$

where $n_{g,p}$ and $n_{g,e}$ are the group indices of the probe and excitation, respectively. Equation (11) is then squared and integrated to find the transmitted energy as a function of temporal delay T_d, which is used to fit the excite-probe measurements for α_3.

Figure 7 shows example measurements of CdS and GaAs, where measurements using multiple excitation energies are used to ensure the quadratic dependence of the signal. For CdS, the excitation and probe wavelengths are significantly different ($\lambda_p = 700$ nm, $\lambda_e = 2.35$ µm) resulting in large GVM, with $\rho = 7.7$ [77]. This results in the broadened signal towards negative delay where the probe reaches the sample first, but the excitation catches up to it within the sample due to its higher group velocity. For the GaAs sample, which is only 4 µm thick, $\lambda_p = 1020$ nm, $\lambda_e = 7.75$ µm, $\rho = 0$, meaning the measurement follows the cross-correlation of the probe pulse and square of the excitation pulse, as there is no temporal walk-off. Fits for the data of Fig. 7 performed using Eq. (11) yield $\alpha_3(\omega_p;\omega_e,\omega_e) = (41 \pm 15)\times 10^{-3}$ cm^3/GW^2 for CdS, and 68 ± 20 cm^3/GW^2 for GaAs, respectively.

Measured 3PA spectra are presented in Fig. 8, where nondegenerate measurements are in red, and degenerate measurements from [22,27] are in black, along with the corresponding theoretical curves. Errors in α_3 stem primarily from uncertainty in the excitation irradiance ($\sim 20\%$). Calculations use the values of E_g, Δ, $\mathbf{E}_p$, and the refractive indices in Table 1. The theoretical

Optics EXPRESS

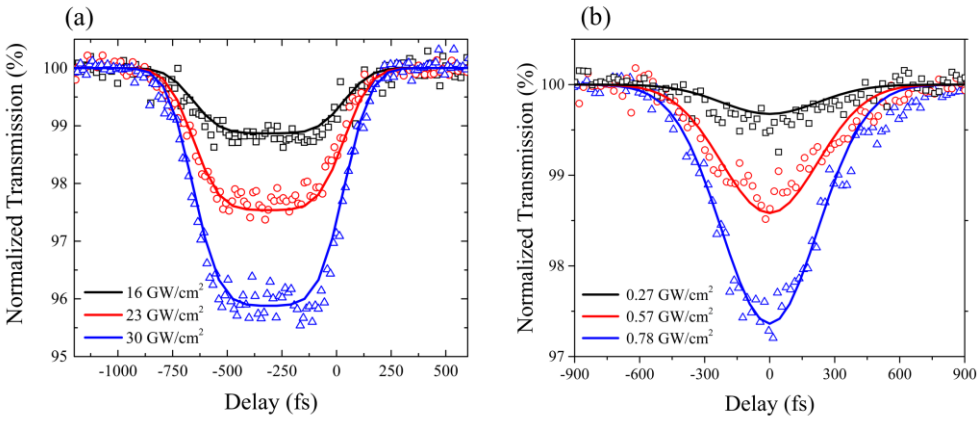

Fig. 7. Examples of (shapes) of excite-probe measurements on (a) CdS ($L = 500\,\mu$m, $\lambda_p = 700$ nm, $\lambda_e = 2.35\,\mu$m, $\rho = 7.7$), and (b) GaAs ($L = 4\,\mu$m, $\lambda_p = 1020$ nm, $\lambda_e = 7.75\,\mu$m, $\rho = 0$) for three different excitation energies with (curves) corresponding fits, where (a) $\alpha_3 = (41 \pm 15) \times 10^{-3}$ cm^3/GW^2, and (b) $\alpha_3 = (68 \pm 20)$ cm^3/GW^2.

predictions for both D-3PA and ND-3PA are multiplied by a constant factor of 3 for GaAs and 1.8 for ZnSe to best match the D-3PA data. This also makes the ND-3PA data fit theory quite well. Similar scaling factors were observed in previous comparisons to theory for both 2PA [35] and 3PA [22]. We observe significant enhancement over the degenerate case for all materials. In GaAs, the maximum enhancement is 180× for $\lambda_p = 1020$ nm and $\lambda_e = 7.75\,\mu$m, ($\hbar\omega_p/\hbar\omega_e = 7.6$), while for ZnSe it is 12× for $\lambda_e = 2.3\,\mu$m and $\lambda_p = 600$ nm ($\hbar\omega_p/\hbar\omega_e = 3.8$). For GaAs and ZnSe there is good agreement between the measured data and the theoretical calculations, particularly for the nondegenerate enhancement, evidenced by the fact that a constant scaling factor is used for the entire spectrum, i.e., both degenerate and nondegenerate. CdS measured here is wurtzite, rather than zinc-blende, which does not have the band structure described by Kane's model. We do, however, still see strong enhancement in CdS for ND-3PA, indicating the universality of the enhancement mechanisms.

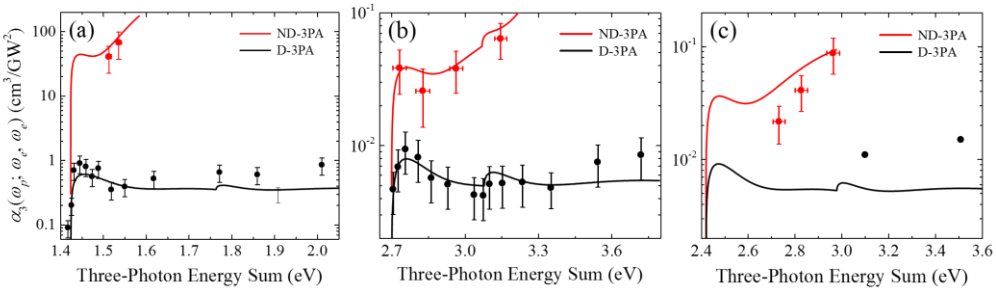

Fig. 8. Comparison of (red) ND-3PA and (black) D-3PA spectra for (a) GaAs, (b) ZnSe, and (c) CdS, including (circles) measurements and (curves) theory. In (a) $\lambda_e = 7.75\,\mu$m (0.16 eV), and theory (both D and ND) is scaled 3×, in (b) $\lambda_e = 2.35\,\mu$m (0.53 eV), and theory (both D and ND) is scaled by 1.8×, and in (c) $\lambda_e = 2.35\,\mu$m with no scaling. D-3PA data from [22,27].

Figure 9 shows the ratio of the 3PA coefficient for parallel and perpendicular polarizations of the excitation and probe, $\alpha_{3,\parallel}/\alpha_{3,\perp}$, which is independent of constant scaling factors. The ratio varies drastically between degenerate and nondegenerate cases, particularly near the band

Optics EXPRESS

edge in ZnSe. This is also very different from the behavior observed in 2PA, where the ratio $\alpha_{2,\parallel}/\alpha_{2,\perp}$ is 2 to 3 across the entire spectrum [34,38]. Experimental measurements for ND-3PA yield agreement in both GaAs and ZnSe.

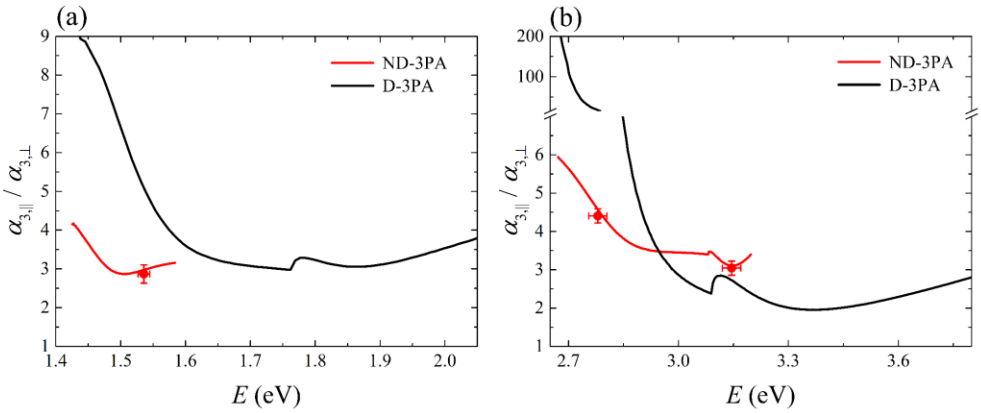

Fig. 9. Polarization dependence of ND-3PA. Calculated (curves) and measured (points) polarization dependence of α_3 (ratio of parallel to perpendicular excitation and probe polarizations) for (a) GaAs and (b) ZnSe for (red) nondegenerate $\lambda_e = 7.75\,\mu$m and $\lambda_e = 2.3\,\mu$m, respectively, and (black) degenerate cases. Note the break in the vertical axis in (b).

5. Conclusion

We have presented calculations of the ND-3PA spectra of zinc-blende semiconductors based on Kane's 8-band model using Fermi's golden rule (third-order perturbation theory). This method shows improved accuracy of the D-3PA spectra over previous two-parabolic band models primarily due to the inclusion of quantum interference between the multiple possible pathways [22,49]. Intermediate-state resonance results in an enhancement of the ND-3PA coefficient for extremely nondegenerate photon pairs, which can be larger than that for ND-2PA thanks to the additional intermediate state involved in the 3PA process; however, in both cases the enhancement due to the 1/ω contribution of the transition matrix elements dominates. This model also provides the polarization dependence of 3PA, which varies rapidly with frequency near the band edge. Excite-probe measurements in the Zinc-blende semiconductors GaAs and ZnSe show good agreement with theory based on the Kane band structure in spectral shape, nondegenerate enhancement including ISRE and the contribution of the 1/ω dependence of the matrix elements, and polarization dependence, indicating that the band structure and tensor symmetry are well accounted for by the model. For wurtzite CdS, the agreement with theory is, as expected, not as good, but experimental results still show similar enhancement of 3PA. The enhancement suggests that ND-3PA may severely limit some photonic applications in bulk semiconductors, such as optical parametric oscillators in the mid-IR [30,31,83], Raman amplifiers [28], supercontinuum sources [5], limits on THz generation [10–12] and nondegenerate two-photon lasers [36,45,46,84,85].

The predicted polarization dependence may be more fully explored, particularly the dramatic increase in $\alpha_{3,\parallel}/\alpha_{3,\perp}$ near the band edge in the degenerate case. This may prove useful for mitigating 3PA as a competing process to two-photon gain for future investigations of two-photon semiconductor lasers [34]. The ND-3PA coefficient may be used to determine the fifth-order nonlinear refractive index (often denoted n_4) via nonlinear Kramers-Kronig relations [78]. The algorithm presented here, along with other fifth-order loss mechanisms, may be used to predict its dispersion. A more accurate model of the band structure [86] may yield better agreement. For

Optics EXPRESS

example, Kane's band structure also assumes α_3 does not depend on the polarization directions with respect to the crystalline axes, though experimental measurements have shown anisotropy of D-3PA [23–25]. Calculations of anisotropy by including higher lying bands and more intricate models of the band structure far from $\mathbf{k} = 0$ are expected to improve accuracy. Impurities, defects, and excitonic effects may play a role as well, particularly near the band edge.

Funding. National Science Foundation (DMR-1609895); DEVCOM Army Research Laboratory (W911NF-15-2-0090).

Acknowledgments. We thank Greg Salamo at the University of Arkansas for the GaAs sample.

Disclosures. The authors declare no conflicts of interest.

Data availability. Data underlying the results presented in this paper are not publicly available at this time but may be obtained from the authors upon reasonable request.

Supplemental document. See Supplement 1 for supporting content.

References

1. B. S. Chris, B. André, and M. Eric, "Laser-induced breakdown and damage in bulk transparent materials induced by tightly focused femtosecond laser pulses," Meas. Sci. Technol. **12**(11), 1784–1794 (2001).
2. C. C. Yang, J. S. Aitchison, A. Villeneuve, *et al.*, "Effects of three-photon absorption on nonlinear directional coupling," Opt. Lett. **17**(10), 710–712 (1992).
3. J. U. Kang, A. Villeneuve, M. Sheik-Bahae, *et al.*, "Limitation due to three-photon absorption on the useful spectral range for nonlinear optics in AlGaAs below half band gap," Appl. Phys. Lett. **65**(2), 147–149 (1994).
4. J. S. Aitchison, D. C. Hutchings, J. U. Kang, *et al.*, "The nonlinear optical properties of AlGaAs at the half band gap," IEEE J. Quantum Electron. **33**(3), 341–348 (1997).
5. R. K. W. Lau, M. R. E. Lamont, A. G. Griffith, *et al.*, "Octave-spanning mid-infrared supercontinuum generation in silicon nanowaveguides," Opt. Lett. **39**(15), 4518–4521 (2014).
6. Z. Wang, H. Liu, N. Huang, *et al.*, "Influence of three-photon absorption on Mid-infrared cross-phase modulation in silicon-on-sapphire waveguides," Opt. Express **21**(2), 1840–1848 (2013).
7. L. Carletti, C. Monat, R. Orobtchouk, *et al.*, "Mid-IR integrated photonics for sensing applications," (2015), pp. 93701J-93701J-93708.
8. C. Husko, S. Combrié, Q. V. Tran, *et al.*, "Non-trivial scaling of self-phase modulation and three-photon absorptionin III-V photonic crystal waveguides," Opt. Express **17**(25), 22442–22451 (2009).
9. C. Husko, P. Colman, S. Combrié, *et al.*, "Effect of multiphoton absorption and free carriers in slow-light photonic crystal waveguides," Opt. Lett. **36**(12), 2239–2241 (2011).
10. M. C. Hoffmann, K.-L. Yeh, J. Hebling, *et al.*, "Efficient terahertz generation by optical rectification at 1035 nm," Opt. Express **15**(18), 11706–11713 (2007).
11. S.-C. Zhong, Z.-H. Zhai, J. Li, *et al.*, "Optimization of terahertz generation from LiNbO3 under intense laser excitation with the effect of three-photon absorption," Opt. Express **23**(24), 31313–31323 (2015).
12. G. Polónyi, B. Monoszlai, G. Gäumann, *et al.*, "High-energy terahertz pulses from semiconductors pumped beyond the three-photon absorption edge," Opt. Express **24**(21), 23872–23882 (2016).
13. C. A. Husko, A. S. Clark, M. J. Collins, *et al.*, "Multi-photon absorption limits to heralded single photon sources," Sci. Rep. **3**(1), 3087 (2013).
14. G. S. He, B. A. Reinhardt, J. D. Bhawalkar, *et al.*, "Three-photon-absorption-induced fluorescence and optical limiting effects in an organic compound," Opt. Lett. **20**(14), 1524–1526 (1995).
15. G. S. He, P. P. Markowicz, T.-C. Lin, *et al.*, "Observation of stimulated emission by direct three-photon excitation," Nature **415**(6873), 767–770 (2002).
16. J. H. Yu, S.-H. Kwon, Z. Petrášek, *et al.*, "High-resolution three-photon biomedical imaging using doped ZnS nanocrystals," Nat. Mater. **12**(4), 359–366 (2013).
17. M. A. Kramer and R. W. Boyd, "Three-photon absorption in Nd-doped yttrium aluminum garnet," Phys. Rev. B **23**(3), 986–991 (1981).
18. D. J. Bamford, L. E. Jusinski, and W. K. Bischel, "Absolute two-photon absorption and three-photon ionization cross sections for atomic oxygen," Phys. Rev. A **34**(1), 185–198 (1986).
19. P. Sałek, H. Ågren, A. Baev, *et al.*, "Quantum Chemical Studies of Three-Photon Absorption of Some Stilbenoid Chromophores," J. Phys. Chem. A **109**(48), 11037–11042 (2005).
20. B. S. Wherrett, "Scaling rules for multiphoton interband absorption in semiconductors," J. Opt. Soc. Am. B **1**(1), 67–72 (1984).
21. H. S. Brandi and C. B. de Araujos, "Multiphonon absorption coefficients in solids: a universal curve," J. Phys. C: Solid State Phys. **16**(30), 5929–5936 (1983).
22. C. M. Cirloganu, P. D. Olszak, L. A. Padilha, *et al.*, "Three-photon absorption spectra of zinc blende semiconductors: theory and experiment," Opt. Lett. **33**(22), 2626–2628 (2008).
23. J. He, Y. Qu, H. Li, *et al.*, "Three-photon absorption in ZnO and ZnS crystals," Opt. Express **13**(23), 9235–9247 (2005).

Optics EXPRESS

24. S. Pearl, N. Rotenberg, and H. M. van Driel, "Three photon absorption in silicon for 2300–3300 nm," Appl. Phys. Lett. **93**(13), 131102 (2008).
25. W. C. Hurlbut, Y.-S. Lee, K. L. Vodopyanov, *et al.*, "Multiphoton absorption and nonlinear refraction of GaAs in the mid-infrared," Opt. Lett. **32**(6), 668–670 (2007).
26. T. Wang, N. Venkatram, J. Gosciniak, *et al.*, "Multi-photon absorption and third-order nonlinearity in silicon at mid-infrared wavelengths," Opt. Express **21**(26), 32192–32198 (2013).
27. C. M. Cirloganu, P. D. Olszak, L. A. Padilha, *et al.*, "Three-photon absorption spectra of zinc blende semiconductors: theory and experiment: erratum," Opt. Lett. **45**(4), 1025–1026 (2020).
28. B. Jalali, V. Raghunathan, R. Shori, *et al.*, "Prospects for Silicon Mid-IR Raman Lasers," IEEE J. Sel. Top. Quantum Electron. **12**(6), 1618–1627 (2006).
29. O. H. Heckl, B. J. Bjork, G. Winkler, *et al.*, "Three-photon absorption in optical parametric oscillators based on OP-GaAs," Opt. Lett. **41**(22), 5405–5408 (2016).
30. K. L. Vodopyanov, O. Levi, P. S. Kuo, *et al.*, "Optical parametric oscillation in quasi-phase-matched GaAs," Opt. Lett. **29**(16), 1912–1914 (2004).
31. P. G. Schunemann, L. A. Pomeranz, and D. J. Magarrell, "Optical parametric oscillation in quasi-phase-matched GaP," (2015), pp. 93470J-93470J-93477.
32. K. L. Vodopyanov, E. Sorokin, I. T. Sorokina, *et al.*, "Mid-IR frequency comb source spanning 4.4–5.4 μm based on subharmonic GaAs optical parametric oscillator," Opt. Lett. **36**(12), 2275–2277 (2011).
33. C. R. Phillips, J. Jiang, C. Mohr, *et al.*, "Widely tunable midinfrared difference frequency generation in orientation-patterned GaAs pumped with a femtosecond Tm-fiber system," Opt. Lett. **37**(14), 2928–2930 (2012).
34. M. Reichert, A. L. Smirl, G. Salamo, *et al.*, "Observation of Nondegenerate Two-Photon Gain in GaAs," Phys. Rev. Lett. **117**(7), 073602 (2016).
35. M. Sheik-Bahae, D. C. Hutchings, D. J. Hagan, *et al.*, "Dispersion of bound electron nonlinear refraction in solids," IEEE J. Quantum Electron. **27**(6), 1296–1309 (1991).
36. C. M. Cirloganu, L. A. Padilha, D. A. Fishman, *et al.*, "Extremely nondegenerate two-photon absorption in direct-gap semiconductors [Invited]," Opt. Express **19**(23), 22951–22960 (2011).
37. M. Sheik-Bahae, J. Wang, and E. W. Van Stryland, "Nondegenerate optical Kerr effect in semiconductors," IEEE J. Quantum Electron. **30**(2), 249–255 (1994).
38. D. C. Hutchings and E. W. V. Stryland, "Nondegenerate two-photon absorption in zinc blende semiconductors," J. Opt. Soc. Am. B **9**(11), 2065–2074 (1992).
39. P. Zhao, M. Reichert, D. J. Hagan, *et al.*, "Dispersion of nondegenerate nonlinear refraction in semiconductors," Opt. Express **24**(22), 24907–24920 (2016).
40. D. A. Fishman, C. M. Cirloganu, S. Webster, *et al.*, "Sensitive mid-infrared detection in wide-bandgap semiconductors using extreme non-degenerate two-photon absorption," Nat. Photonics **5**(9), 561–565 (2011).
41. H. S. Pattanaik, D. A. Fishman, E. W. Van Stryland, *et al.*, "Pulsed and CW IR Detection in Wide-gap Semiconductors using Extremely Nondegenerate Two-photon Absorption," in *CLEO: 2013* (Optical Society of America, San Jose, California, 2013), p. CTu3E.3.
42. H. Pattanaik, D. Fishman, S. Webster, *et al.*, "IR detection in wide-gap semiconductors using extreme nondegenerate two-photon absorption," in *CLEO:2012* (*Optical Society of America*2012), p. QF2 G.7.
43. H. S. Pattanaik, R. Matthew, D. J. Hagan, *et al.*, "Three-dimensional IR imaging with uncooled GaN photodiodes using nondegenerate two-photon absorption," Opt. Express **24**(2), 1196 (2016).
44. D. Knez, A. M. Hanninen, R. C. Prince, *et al.*, "Infrared chemical imaging through non-degenerate two-photon absorption in silicon-based cameras," Light: Sci. Appl. **9**(1), 125 (2020).
45. C. N. Ironside, "Two-photon gain semiconductor amplifier," IEEE J. Quantum Electron. **28**(4), 842–847 (1992).
46. D. J. Gauthier, "Two-photon lasers," in *Progress in Optics*, E. Wolf, ed. (Elsevier Science & Technology, 2003), pp. 205–272.
47. N. Cox, J. Wei, H. Pattanaik, *et al.*, "Nondegenerate two-photon absorption in GaAs/AlGaAs multiple quantum well waveguides," Phys. Rev. Res. **2**(1), 013376 (2020).
48. E. O. Kane, "Band structure of indium antimonide," J. Phys. Chem. Solids **1**(4), 249–261 (1957).
49. S. Benis, C. M. Cirloganu, N. Cox, *et al.*, "Three-photon absorption spectra and bandgap scaling in direct-gap semiconductors," Optica **7**(8), 888–899 (2020).
50. M. Sheik-Bahae, A. A. Said, T. H. Wei, *et al.*, "Sensitive measurement of optical nonlinearities using a single beam," IEEE J. Quantum Electron. **26**(4), 760–769 (1990).
51. A. E. Kaplan, ""External" self-focusing of light by a nonlinear layer," Radiophys. Quantum Electron. **12**(6), 692–696 (1969).
52. G. I. Stegeman and R. A. Stegeman, *Nonlinear Optics: Phenomena, Materials and Devices* (John Wiley & Sons, Inc., 2012).
53. R. A. Negres, J. M. Hales, A. Kobyakov, *et al.*, "Experiment and analysis of two-photon absorption spectroscopy using a white-light continuum probe," IEEE J. Quantum Electron. **38**(9), 1205–1216 (2002).
54. J. K. Wahlstrand, J. H. Odhner, E. T. McCole, *et al.*, "Effect of two-beam coupling in strong-field optical pump-probe experiments," Phys. Rev. A **87**(5), 053801 (2013).
55. P. N. Butcher and C. David, *The Elements of Nonlinear Optics* (Cambridge University Press, 1990).

Optics EXPRESS

56. M. C. Reichert, "Nonlinear Optical Response of Simple Molecules and Two-Photon Semiconductor Lasers," (University of Central Florida, 2015).
57. P. Meystre and M. Sargent, *Elements of quantum optics* (Springer Science & Business Media, 2007).
58. M. Born, *Atomic physics* (Courier Corporation, 1989).
59. H. S. Pattanaik, M. Reichert, J. B. Khurgin, *et al.*, "Enhancement of Two-photon Absorption in Quantum Wells for Extremely Nondegenerate Photon Pairs," IEEE J. Quantum Electron. (Submitted 2015).
60. J. Rioux, G. Burkard, and J. E. Sipe, "Current injection by coherent one- and two-photon excitation in graphene and its bilayer," Phys. Rev. B **83**(19), 195406 (2011).
61. N. S. Makarov, P. C. Lau, C. Olson, *et al.*, "Two-Photon Absorption in CdSe Colloidal Quantum Dots Compared to Organic Molecules," ACS Nano **8**(12), 12572–12586 (2014).
62. M. Drobizhev, A. Karotki, M. Kruk, *et al.*, "Resonance enhancement of two-photon absorption in porphyrins," Chem. Phys. Lett. **355**(1-2), 175–182 (2002).
63. K. Kamada, K. Ohta, Y. Iwase, *et al.*, "Two-photon absorption properties of symmetric substituted diacetylene: drastic enhancement of the cross section near the one-photon absorption peak," Chem. Phys. Lett. **372**(3-4), 386–393 (2003).
64. J. M. Hales, D. J. Hagan, E. W. Van Stryland, *et al.*, "Resonant enhancement of two-photon absorption in substituted fluorene molecules," J. Chem. Phys. **121**(7), 3152–3160 (2004).
65. T. R. Ensley, H. Hu, M. Reichert, *et al.*, "Quasi 3-level Model Applied to Measured Spectra of Nonlinear Absorption and Refraction in Organic Molecules," Journal of the optical Society of America B (to be submitted).
66. J. E. Bjorkholm and P. F. Liao, "Resonant Enhancement of Two-Photon Absorption in Sodium Vapor," Phys. Rev. Lett. **33**(3), 128–131 (1974).
67. S. L. Chuang, *Physics of Optoelectronic Devices* (Wiley-Interscience, 1995).
68. J. S. Blakemore, "Semiconducting and other major properties of gallium arsenide," J. Appl. Phys. **53**(10), R123–R181 (1982).
69. I. Vurgaftman, J. R. Meyer, and L. R. Ram-Mohan, "Band parameters for III–V compound semiconductors and their alloys," J. Appl. Phys. **89**(11), 5815–5875 (2001).
70. P. F. Liao, P. Kelley, and P. S. Zory Jr, *Quantum Well Lasers* (Elsevier, 2012).
71. T. Skauli, P. S. Kuo, K. L. Vodopyanov, *et al.*, "Improved dispersion relations for GaAs and applications to nonlinear optics," J. Appl. Phys. **94**(10), 6447–6455 (2003).
72. H. Morkoç, S. Strite, G. B. Gao, *et al.*, "Large-band-gap SiC, III-V nitride, and II-VI ZnSe-based semiconductor device technologies," J. Appl. Phys. **76**(3), 1363–1398 (1994).
73. D. J. Chadi, "Spin-orbit splitting in crystalline and compositionally disordered semiconductors," Phys. Rev. B **16**(2), 790–796 (1977).
74. E. W. Van Stryland, M. A. Woodall, H. Vanherzeele, *et al.*, "Energy band-gap dependence of two-photon absorption," Opt. Lett. **10**(10), 490–492 (1985).
75. B. Tatian, "Fitting refractive-index data with the Sellmeier dispersion formula," Appl. Opt. **23**(24), 4477–4485 (1984).
76. W. E. Bron, *Ultrashort processes in condensed matter* (Springer Science & Business Media, 2012).
77. M. S. Gomez, J. M. Guerra, and F. Vilches, "Weighted nonlinear regression analysis of a Sellmeier expansion: comparison of several nonlinear fits of CdS dispersion," Appl. Opt. **24**(8), 1147–1150 (1985).
78. D. C. Hutchings, M. Sheik-Bahae, D. J. Hagan, *et al.*, "Kramers-Krönig relations in nonlinear optics," Opt. Quant. Electron. **24**(1), 1–30 (1992).
79. M. R. Ferdinandus, H. Hu, M. Reichert, *et al.*, "Beam deflection measurement of time and polarization resolved ultrafast nonlinear refraction," Opt. Lett. **38**(18), 3518–3521 (2013).
80. M. Reichert, H. Hu, M. R. Ferdinandus, *et al.*, "Temporal, spectral, and polarization dependence of the nonlinear optical response of carbon disulfide," Optica **1**(6), 436–445 (2014).
81. M. Reichert, P. Zhao, J. M. Reed, *et al.*, "Beam deflection measurement of bound-electronic and rotational nonlinear refraction in molecular gases," Opt. Express **23**(17), 22224–22237 (2015).
82. D. Milam, "Review and Assessment of Measured Values of the Nonlinear Refractive-Index Coefficient of Fused Silica," Appl. Opt. **37**(3), 546–550 (1998).
83. V. Petrov, "Frequency down-conversion of solid-state laser sources to the mid-infrared spectral range using non-oxide nonlinear crystals," Prog. Quantum Electron. **42**, 1–106 (2015).
84. A. Nevet, A. Hayat, and M. Orenstein, "Measurement of Optical Two-Photon Gain in Electrically Pumped AlGaAs at Room Temperature," Phys. Rev. Lett. **104**(20), 207404 (2010).
85. A. Hayat, P. Ginzburg, and M. Orenstein, "Observation of two-photon emission from semiconductors," Nat. Photonics **2**(4), 238–241 (2008).
86. D. C. Hutchings and B. S. Wherrett, "Theory of anisotropy of two-photon absorption in zinc-blende semiconductors," Phys. Rev. B **49**(4), 2418–2426 (1994).